Design of a metallic glass dispersion in pure copper by friction stir processing

Marie-Noëlle Avettand-Fènoël, N. Netto, A. Simar, Maya Marinova, R. Taillard

HAL Id: hal-03614666

https://hal.univ-lille.fr/hal-03614666v1

Submitted on 22 Jul 2024

Design of a metallic glass dispersion in pure copper by friction stir processing

M.-N. Avettand-Fènoël[1,*], N. Netto[2], A. Simar[2], M. Marinova[3], R. Taillard[1]

[1] Univ. Lille, CNRS, INRAE, Centrale Lille, UMR 8207 – UMET – Unité Matériaux et Transformations, F-59000 Lille, France
[2] UCLouvain, Institute of Mechanics, Materials and Civil Engineering, IMAP, B-1348 Louvain La Neuve, Belgium
[3] Univ. Lille, CNRS, INRAE, Centrale Lille, Univ. Artois, FR 2638, IMEC - Institut Michel-Eugène Chevreul, F-59000, Lille, France

* Corresponding author, e-mail: Marie-Noelle.Avettand-Fenoel@univ-lille.fr
Tel: 33(0)320436927, Fax: 33(0)320434040

Abstract

Multipass friction stir processing of Fe based metallic glass ribbons interspersed between Cu plates was performed. From the first pass, the process entailed on the one hand the decrease of the Cu mean grain size in the nugget by a factor of about 5 and on the other hand the fracture, the refinement and the partial crystallization of the amorphous reinforcement ~~from the first pass~~. Cu diffusion also led to marked Cu enrichments in the Fe based metallic glass whose mean Cu content reached 2.7 at.%. Beside the metallic glass based reinforcements, some nanometric polycrystalline copper oxides were formed and dispersed within the nugget. The nugget also experienced dynamic recovery and dynamic recrystallization which was in particular favored by the accumulation of dislocations around the reinforcements. Finally, the greater number of passes, the harder the nugget becomes.

1. Introduction

Copper is used in many applications requiring high thermal and/or high electrical conductivity such as electronic connectors and heat sinks. However, it suffers from low mechanical resistance. Two solutions using friction stir welding (FSW), or its friction stir processing (FSP) derivative, have been implemented to improve the mechanical or functional performances of Cu. The first one consists in refining the Cu microstructure by FSW or FSP **[1-6]** eventually with additional cooling **[7-9]** and an increased number of passes **[8]**. An attractive ductility-strength combination was obtained in the latter case. The second one is concerned by the development by FSP of Cu based metal matrix composites (MMCs) reinforced either with yttria **[10]**, with TiC, B_4C, WC, Al_2O_3 **[11]** or with SiC **[12-17]** showing for instance an enhanced wear resistance **[11]**. However, no study deals with Cu based composite reinforced with metallic glass and further produced by a solid state process.

1

Literature only reports some studies dealing with the association of metals and metallic glasses via joining. These latter ~~literature~~ works are concerned with

i)   diffusion bonding of AA1050 to $Cu_{50}Zr_{43}Al_7$ bulk metallic glass (BMG) at temperatures under the glass transition temperature which gives rise to the formation of ~~an~~ $CuAl_2O_4$ interfacial ~~$CuAl_2O_4$~~ diffusion layer [18] and

ii)   butt friction stir joints of alloys with metallic glass, i.e. a Cu - $Zr_{55}Cu_{30}Al_{10}Ni_5$ BMG [19] and an Al-Zn-Mg-Cu alloy - $Zr_{55}Cu_{30}Al_{10}Ni_5$ BMG [20] weldment.

The present study is an early step for the design and development by FSP of a Cu based matrix composite reinforced with a metallic glass. ~~As~~ FSW/FSP proceeds at a ~~the~~ 0.6-0.7 homologous temperature defined as ~~the absolute processing temperature divided by the absolute melting temperature of the material~~ the ratio between the processing and the melting temperature (absolute values), ~~close to 0.6-0.7, this corresponds to~~ that is to say at a ~~welding~~ temperature in-between 541 and 677°C for Cu. This processing condition requires to identify a suitable metallic glass with phase transformation temperatures over this range. The $Fe_{64}B_{24}Y_4Nb_6Al_{0.4}$ metallic glass seems convenient ~~as it presents a~~ with its 585±2°C glass transition (T_g) and ~~a~~ 677±2°C onset primary crystallization (T_x) temperature at a heating rate of $10°C.s^{-1}$ [21]. The association of Cu with the $Fe_{64}B_{24}Y_4Nb_6Al_{0.4}$ metallic glass is thus expected to combine the high thermal and electrical conductivities of Cu with the specific properties of the metallic glass, in particular its high hardness at the amorphous or crystallized state [21], and its ferromagnetic behavior if partially amorphous. It will thus enable to obtain a good compromise of properties for the composite governed by the structural state of the metallic glass generated by FSP.

In the present paper, the hardness of the reinforcement after FSP, which is directly linked to its state ~~(amorphous, partially or fully crystallized)~~ will thus be more particularly analyzed. Indeed, the glass may remain amorphous or become a supercooled liquid or even a more or less partially crystallized phase. High temperature leads to partial crystallization if the glass is held in the supercooled liquid region for a duration of almost 1 min [22] or if it reaches a temperature higher than the onset temperature of primary crystallization ~~temperature~~. A short holding of the metallic glass at a high temperature can overbalance the longer incubation time required for its crystallization at a lower temperature. As Cu presents a high thermal diffusivity, the thermal conditions undergone by the metallic glass during processing may nevertheless differ from those expected. In addition, the high deformation and strain rate generated during FSP may further modify the behavior of the metallic glass by reducing its glass and primary crystallization temperatures.

Another topic will concern the behavior, under the combined effect of temperature and deformation, of both Cu and Fe, which is the major element of the metallic glass since the Fe-Cu heat of mixing is positive and amounts to 13 kJ/mol [23].

In summary, the effect of FSP on the phase transformations, on material flow in the Cu based material and on its hardness will be investigated.

2. Experimental procedure

The base materials are 150 x 40 x 5 mm^3 Cu-a1 pure copper (hardness of 81 $HV_{0.05}$) plates and about 50 mm long, 50 µm thick and 2 mm wide $Fe_{64}B_{24}Y_4Nb_6Al_{0.4}$ metallic glass (MG) ribbons (hardness of 1027 $HV_{0.05}$ for the bulk state).

Two configuration settings displayed in Fig. 1a were used. In the first one, a metallic glass ribbon was stuck with glue to the middle of the upper surface of a 5 mm thick Cu plate and a 0.7 µm thick Cu rolled foil was placed over the latter stacking to avoid any loss of MG ribbon during FSP. In the second one and for comparison, the stacking does not contain any

MG ribbon; it only comprises the 5 mm thick Cu plate covered by the 0.7 µm thick top Cu rolled plate. The plates stackings are firmly maintained by the stainless steel clamping system and no backing plate between the clamping system and the specimen was used.
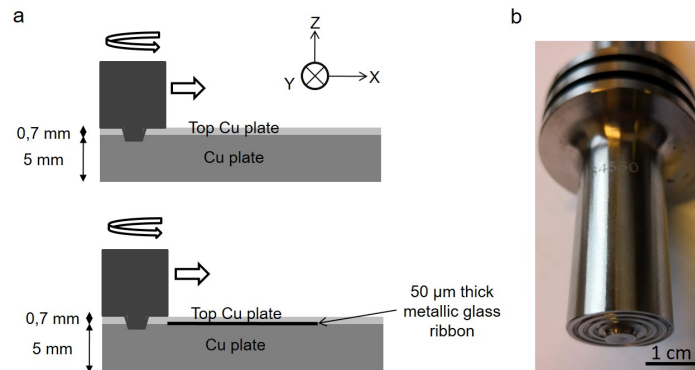

Figure 1: Schematics of FSP setting without and with the metallic glass ribbon (a) and tool features (b).

Friction stir processing (FSP) was controlled in position and performed under an argon flow. The 20 mm diameter scrolled shoulder was prolonged by a truncated and unthreaded pin with a 6 mm root diameter and a 1.5 mm length (Fig. 1b). The tool, made of H13 steel, was backwards tilted with an angle of 1° and its penetration depth was 1.6 mm. Processing speed was 40 mm/min and a 500 rpm anticlockwise rotational speed was used. 1 or 3 overlapping FSP passes were carried out with a dwell time of 10 minutes in-between passes. For the multipass cases, the tool path was chosen in order to maintain the advancing side always on the same side. Forces were also recorded during processing. In the following, the abbreviations "Cu – no MG – number of passes" stand for the specimens without MG and "Cu – MG – number of passes" for those with MG.

The samples were mounted along their transverse cross section, ground on progressively finer SiC papers to a 4000 grit finish and polished using 6 µm, 3 µm and 1 µm diamond paste. The global views of the samples were observed by light microscopy after electrolytic polishing with a solution of 70 vol.% orthophosphoric acid and 30 vol.% glycerine under 2 V at 12°C for 50 s with a current density of 0.35 A.cm⁻². Electrolytic etching was then performed with the same solution, current density, flux and temperature for 55 s under 0.5 V.

The chemical composition of the reinforcements was identified by Electron Probe Micro Analysis (EPMA) and Wavelength Dispersive Spectroscopy (WDS) with a Cameca SX100[TR] equipment while the crystallography of the crystallized second phases was supplied by X-ray diffraction analyses with a Cu anticathode (λ_{Cu} = 1.5406 Å) and a Bragg-Brentano configuration using a Rigaku Smartlab[TR] diffractometer.

Texture components were identified by Electron Back Scattered Diffraction (EBSD) analyses using a Hitachi SU5000[TR] field emission gun scanning microscope. For this purpose, final polishing was done with an ethylic alcohol and dry OPS suspension solution using a VibroMet 2 vibratory polisher with a vibrational magnitude of 10% for 2 hours or manually with OPS suspension followed by ionic polishing. EBSD data have been analyzed using the ATEX software [24].

Several thin foils were prepared by focused ion beam (FIB) with a FEI Strata DB 235[TR] device. They were mounted on FIB molybdenum grids. The thin foils were then analyzed by transmission electron microscopy (TEM) using a FEI Tecnai[TR] G2 20 twin microscope under a 200 kV accelerating voltage equipped with a Scanning (S) TEM / Energy

Dispersive Spectroscopy (EDX) system. Thin foils were also observed by high resolution scanning transmission electron microscopy (HR-S/TEM) by means of a ThermoFisher Titan Themis 300[TR] microscope, equipped with a probe aberration corrector. Scanning TEM (STEM) observations were carried out with an accelerating voltage of 200 kV with a spot size of about 500 pm, semi-convergence angle of 21 mrad and probe current of approximately 100 pA. High angle annular dark field (HAADF) images were recorded with collection angles ranging from 50 mrad to 200 mrad. A super-X windowless 4 quadrant SDD (silicon drift detector) detection system was also used for the STEM-EDX mapping. The microscope is equipped with a high resolution post-column GIF, i.e. the GATAN's Quantum ERS/966 with 2kx2k Ultrascan camera with 994G sensor type, for the acquisition of electron energy loss spectra (EELS). Dual EELS acquisition was performed in the spectral imaging mode with a 49 mrad collection angle ~~of 49 mrad~~, a dispersion of 0.5 eV per channel over the 400 to 1400 eV ~~and covering~~ energy range ~~between 400 eV and 1400 eV~~, a step of 6 Å, and a dwell time of approximately 100 ms. Alignment of the energy drift was done on the zero-loss peak. Such characterizations enabled to determine the effect of processing on the local chemical composition and structure of the metallic glass and on the eventual diffusion phenomena at the atomic scale.

Some Vickers microhardness tests under a 50 g load were finally performed with a Buehler[TR] equipment on the transverse sections of the specimens with a measurement step of 500 µm along the Y axis and 1 mm along the Z axis, respectively (Fig. 1a).

3. Results

3.1. Base materials

In the transverse cross section, the Cu base material presents some rather polygonal grains with a mean size close to 14.6 µm ~~(and a size distribution in-between 6 and 111 µm)~~ (Fig. 2a). As indicated by the 25.9 length % of twin boundaries, these ~~These~~ grains contain many twins of growth ~~(25.9 length % of twin boundaries)~~ (Fig. 2a). Processing and annealing may indeed introduce a large amount of twin boundaries in Cu [25-27].

In accordance with previous X-ray diffractometry investigations [21-22], the quenched metallic glass exhibits the typical features of an amorphous state ~~as seen from~~ proved by the HRTEM images and selected area electron diffraction patterns (Fig. 2b).
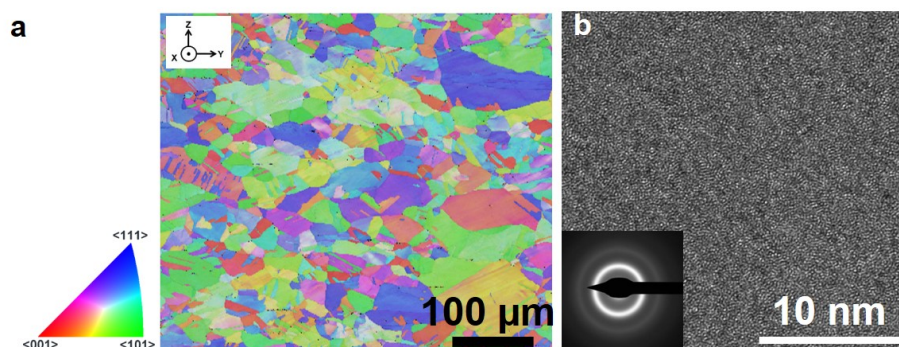

Figure 2: Inverse pole figure (IPFZ) map overlapped with the band contrast map of the transverse cross section of the Cu base material (EBSD) (a) and HRTEM image with selected area electron diffraction pattern of the $Fe_{64}B_{24}Y_4Nb_6Al_{0.4}$ metallic glass (b).

3.2. Evolution of forces and torque during processing

Fig. 3 displays the evolution of both the axial torque and force along the Z vertical direction recorded during the process *vs.* the sample nature. The presence of the metallic glass in the sample leads to a decrease of both the F_z vertical force and the torque during the first pass (Fig. 3b and e). In presence of MG, an increase of the passes number leads to a reduction of the Fz oscillations amplitude (Fig. 3c) and to the vanishing of the MG effect on the torque (Fig. 3f).
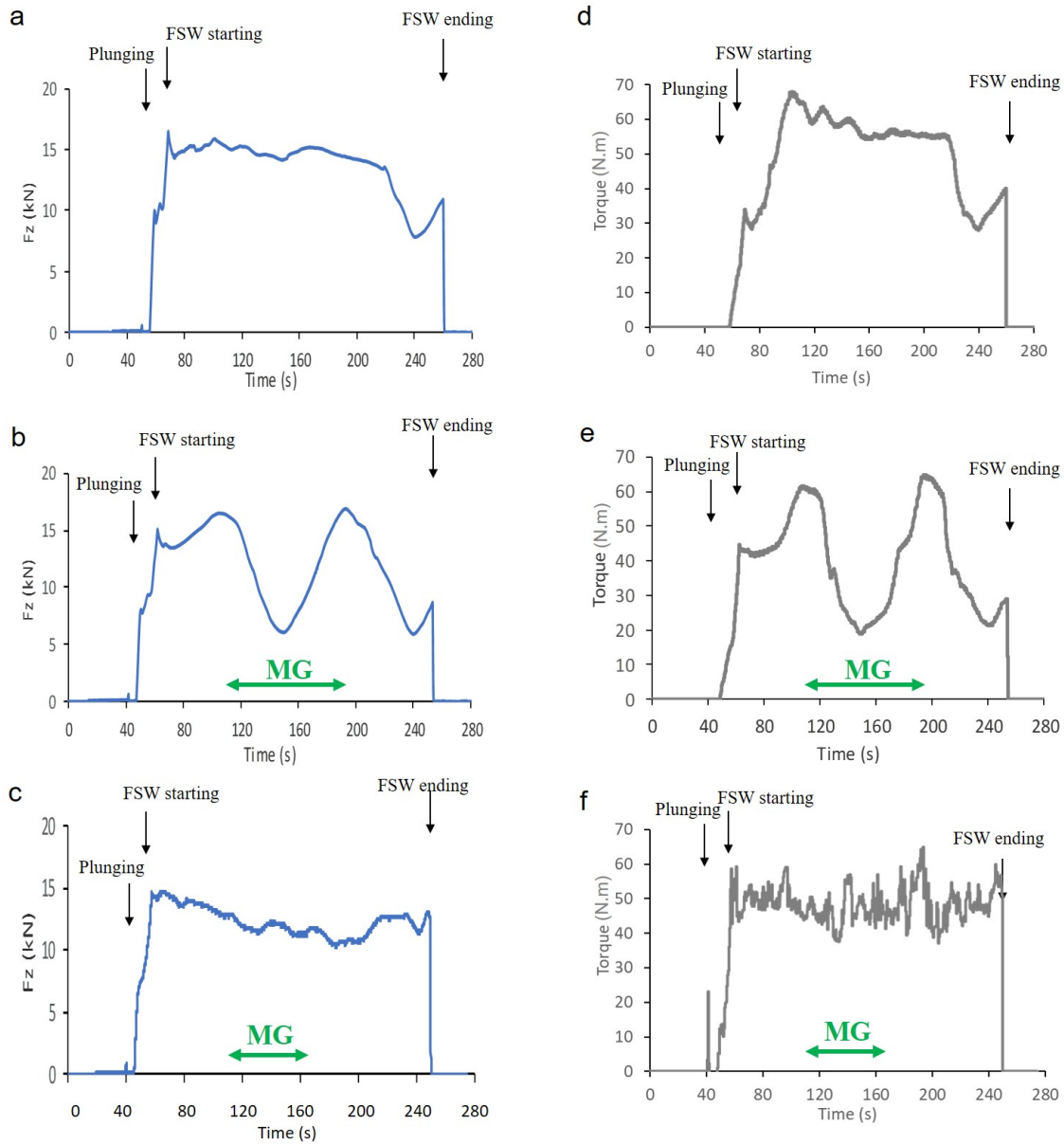

Figure 3: Evolution of the F_z force along the Z axial direction and of the tool torque during the process for the Cu-no MG-1 (a,d), Cu-MG-1 (b,e) and Cu-MG-3 (c,f) sample, respectively. According to both the location of the MG ribbon in the sample setting and the processing

speed, the MG ribbon location has been correlated to the processing time for the Cu-MG-1 and Cu-MG-3 cases.

3.3. Microstructure of the friction stir processed samples

3.3.1. Samples surface
The global views of the samples top surfaces (Fig. 4a-c) indicate the presence of flash on both sides of the tool route and whatever the sample. Some holes (marked by yellow arrows in Fig. 4b) are also noticed at the surface of the Cu-MG-1 sample while they disappear with an increase of the number of passes (Fig. 4c).

3.3.2. Various zones
~~According to their~~ In transverse cross-sections, the samples present various zones, namely a nugget surrounded successively by a heat affected zone (HAZ) ~~bordered by~~ and the base material. Electrolytical etching put into evidence the nugget while the frontier between the HAZ and the base material is far less obvious in Fig. 4d-e-f. ~~Along~~ In this cross-section and based on the intercept method, the heat affected zone presents a mean grain size of 138 µm in Cu-no MG-1 *vs.* 183 µm in Cu-MG-1 and 152 µm in Cu-MG-3. It is worth noting that no thermo-mechanically affected zone (TMAZ) was obviously identified, which is consistent with previous studies of friction stir welded copper [28].

After the first FSP pass (Fig. 4d-e), the presence of metallic glass leads to a wider nugget. In addition, an increase of the number of passes reduces the nugget ~~extent along the sample~~ depth (Fig. 4e-f).
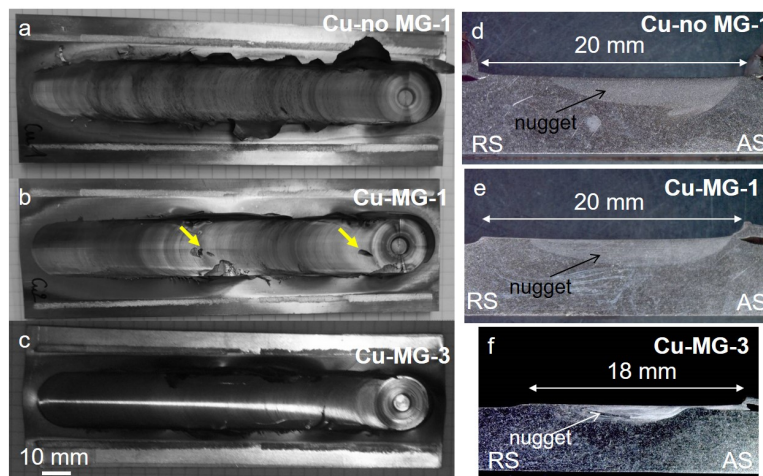

Figure 4: Plane views of the joint top surface (a-c) and transverse cross section (YZ plane) after electrolytical etching (d-f) of the samples (a,d: Cu-no MG-1 ; b,e: Cu-MG-1 ; c,f: Cu-MG-3).

Light microscopic analyses (not shown here) exhibit that the grains in the Cu-no MG-1 nugget~~, the grains~~ are equiaxed ~~and the~~ with a close to 22.2 µm mean ~~grain~~ size ~~is about 22.2 µm (with~~ and a [5.3-71.5 µm] width of size distribution~~) according to light microscopic analyses (not shown here)~~. The nugget of the MG bearing samples comprises bands of polygonal and most often equiaxed grains (Fig. 5a-b). In the Cu-MG-1 case (Fig 5a), the bands are composed of grains differing by their size because of heterogeneous recrystallization ~~in the Cu-MG-1 case (Fig 5a)~~. The Cu average grain size is 3.4 µm, with a

size distribution in-between 1.2 and 41.9 µm, in the Cu-MG-1 nugget *vs.* 1.9 µm, with a size distribution in-between 1.6 and 23.5 µm, in the Cu-MG-3 nugget.

Fig. 5c also exhibits the texture components of the Cu base material and of the Cu-MG-1 and Cu-MG-3 nuggets ~~after FSP~~.

With regard to the Cu base material, its main texture components are {-111}<-1-10> Ab, {-100}<0-10> Cb (Cube), {-213}<-3-64> S3, {-112}<-1-11> Cu (Copper) and {-4 4 11}<-11 -11 8> Ty (Dillamore). The S3 and Cu texture components are indeed observed in rolled face cubic centered (fcc) metals [29]. In addition, Cb and S3 are the components of recrystallization textures in fcc metals [29]. The presence of a significant quantity of annealing twins (Fig. 2a and 5d) which are formed during an advanced state of recrystallization process confirms the occurrence of the latter phenomenon during rolling.

In the nugget after one FSP pass and in presence of reinforcement, the {-111}<-1-10> Ab, {-1-11}<112> A1, {-112}<110> B and {11-1}<112> A2 shear texture components are dominating, compared to the shear {-101}<-1-2-1> Bs and recrystallization {-101}<0-10> Gs texture components in fcc metals [29]. After three FSP passes, the {-112}<110> B and {1-1-1}<110> A shear texture components are far predominant together with {-100}<0-10> Cb (Cube) to a lesser extent (Fig. 5c). According to Liu *et al* [1], A and Ab texture components tend to develop at high strain rates while the B, Bb and C components form at low strain rates in FSWed Cu due to the self-adaptation of the crystallographic orientation to the local changes of ~~the~~ strain rate and ~~the~~ flow stress. A and Ab shear texture components were for instance shown to dominate in the nugget of pure copper friction stir processed at cryogenic temperatures [5].

Fig. 5d gives the length percentage of high angle grain boundaries (HAGB), low angle grain boundaries (LAGB) and twin boundaries (Σ3) in the base material and in the nuggets after 1 and 3 FSP passes, respectively. HAGBs are the predominant boundaries irrespective of the material. An increase of the HAGB ~~volume~~ fraction can be noted in the nuggets compared to the base material, which suggests the occurrence of dynamic recrystallization during FSP. Another proof of the effectiveness of dynamic recrystallization is given by Fig 5e which exhibits an annealing twin in the Cu-MG-3 nugget. By way of contrast, and in ~~agreement~~ accordance with a higher degree of advancement of recrystallization, the length percentage of twin boundaries is about 10 times greater in the base material compared to the nuggets. The low frequency of twins in the nuggets suggests that twinning does not play a major role in the microstructure refinement during FSP. Besides, Fig. 5f indicates that the average grain misorientation in the nuggets after 1 and 3 passes is essentially below 2°, which proves the occurrence of the first step of dynamic recrystallization, namely dynamic recovery ~~during FSP~~. Such a conclusion is consistent with the observation of dislocation cells, for instance in the i encircled area in Fig. 10h. It is however a priori surprising because of the rather low stacking fault energy of Cu. The recovery occurrence is very likely ~~related~~ due to the promotion of atomic diffusion phenomena. Short-circuit diffusion may indeed happen as very drastic plastic strain ranging from 2 to approximately 130 are predicted to occur in local areas of the nugget [30-35]. The effectiveness of deformation induced diffusion is the more likely as local and transient high supersaturations of vacancies are generated at high strain rates [36-37] and in particular at the 1 to 650 s^{-1} values commonly assessed during FSW [30,33,35,38-44].
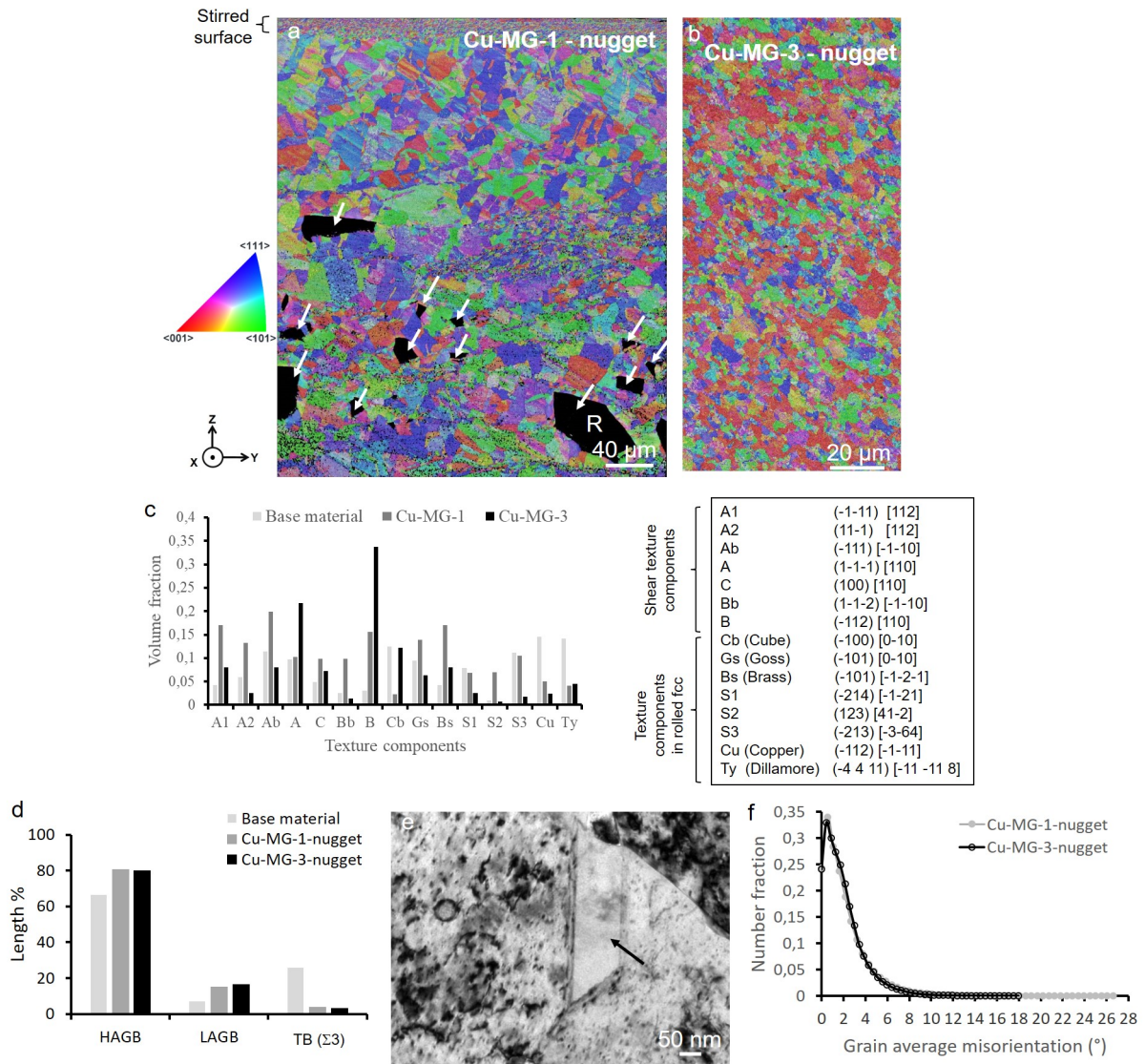
Figure 5: Inverse pole figure (IPFZ) of Cu overlapped with band contrast map in the nuggets of the Cu-MG-1 (a) [the white arrows indicate the presence of reinforcement debris] and of the Cu-MG-3 sample (b), respectively. Repartition of the texture components in the base material, and in the nuggets of the Cu-MG-1 and Cu-MG-3 samples, respectively (c). Grain boundaries distribution [HAGB and LAGB with an angular misorientation greater than 15° and in-between 5 and 15°, respectively] (d). Twin (marked by a black arrow) within the Cu-MG-3 nugget (TEM) (e). Grain boundary fraction *vs.* grain average misorientation (f).

3.3.3. Material flow

~~First of all~~Firstly, it is worth noting the absence of onion rings in the nuggets. Similar observations have already been reported by using an unthreaded probe as in the present case [4,19]. Secondly, the material flow during ~~welding~~ stirring is affected by the presence of the metallic glass. The metallic glass ribbon was fragmented into more or less big pieces by the FSP tool. According to their size, these fragments disturbed more or less the heterogeneous material flow around the tool. In the Cu-MG-3 nugget, Fig. 6b and 6c show for instance different bands with either small or coarse Cu grains. As usual in friction stirring, these zones result from distinct flow bands with different levels of deformation. The deformation was concentrated in zones where small grains have formed by dynamic recrystallization while the zones with the coarser grains have experienced less deformation, or the reverse as coarse

grains can also result from a faster recrystallization. After three passes, the meticulous examination of the flow lines on the retreating side in the nugget transverse cross section reveals some vortices around particles of reinforcement with a size of 10 or 30 µm (Figs 6a to 6c). In addition, the smallest reinforcement pieces are obviously surrounded by small and even nanometric Cu grains as exemplified by the Cu-MG-3 sample (Fig. 6d). Fig. 6e confirms that these nanometric grains delimited by high angle grain boundaries result from dynamic recrystallization.
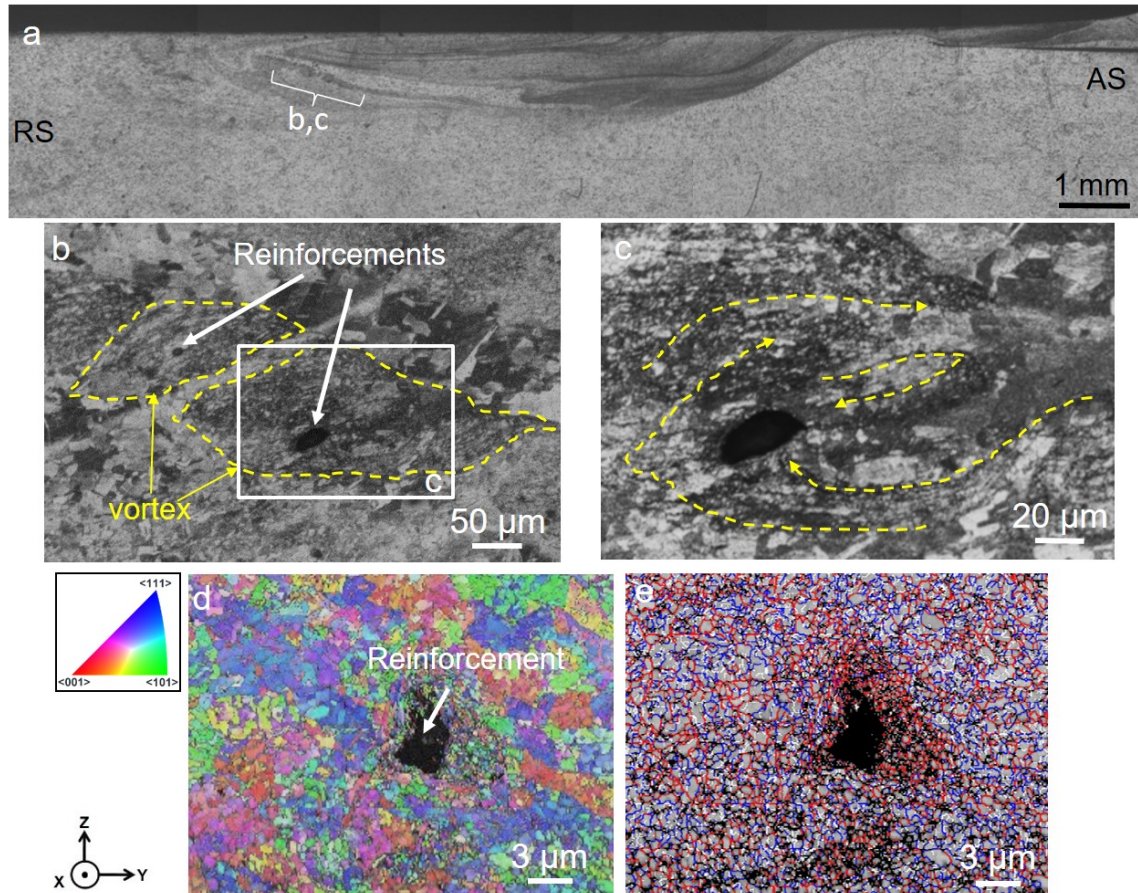

Figure 6: Transverse cross section of the Cu-MG-3 nugget after electrolytical etching (a): material flow lines and vortices in the vicinity of reinforcement pieces (b,c), inverse pole figure (IPFZ) of Cu overlapped with the band contrast map around another fragment of reinforcement (d), boundaries distribution (white, blue and red color for boundaries with angular misorientation below 5°, in-between 5 and 15° and greater than 15°, respectively) at the same place (e). The white arrow in figure d indicates the reinforcement piece.

3.3.4. Distribution, morphology, size and nature of the second phases

3.3.4.1. Distribution

According to the Cu-MG-1 SEM analyses, some reinforcement pieces were observed up to a distance of 622 µm below the top layer and over a width of 2.35 mm. This extent is greater than the 2 mm width of the primitive metallic glass ribbon. With an increase of the passes number, the second phases are observed over a larger area delimited by a 1.12 mm depth from the top layer and an 8.12 mm width in the Cu-MG-3 sample. Given these SEM observations, the nugget area (Fig. 4d-f) and the dimensions of the initial MG ribbon, the volume fraction of

9

reinforcements is very likely around 6.4% and 1% in the zones of dispersion within the Cu-MG-1 and the Cu-MG-3 sample, respectively.

3.3.4.2. Morphology and size at the micrometric scale

After the first pass, the angular shaped reinforcements are either elongated or equiaxed in the (Y-Z) plane (Fig. 7); they present a monomodal distribution with an 18.2 µm mean size and a 3.8 µm mode. After 3 passes, there remains few coarse and ragged reinforcements with a size up to 50 µm (Fig. 7) plus at a finer scale, a rather dense and homogeneous dispersion of spheroidal nanometric fragments (Fig. 8).
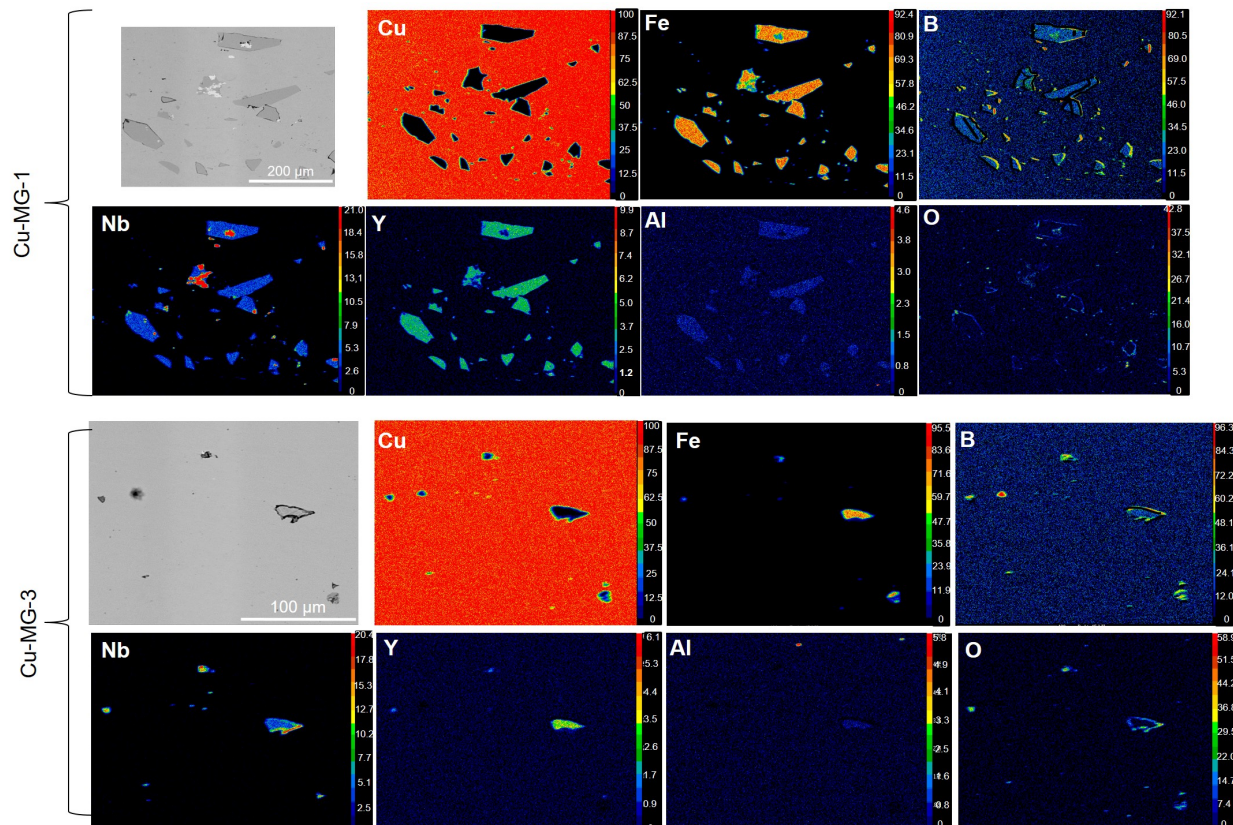

Figure 7: Back scattering electrons (BSE) micrographs displaying the reinforcements dispersion in the (YZ) transverse section of the Cu-MG-1 and Cu-MG-3 specimens, respectively. The Cu Kα, Fe Kα, B Kα, Nb Kα, Y Kα, Al Kα and O Kα X-ray maps (WDS/EPMA) of the same zones are also presented. The color bars indicate the atomic percents of the chemical elements.
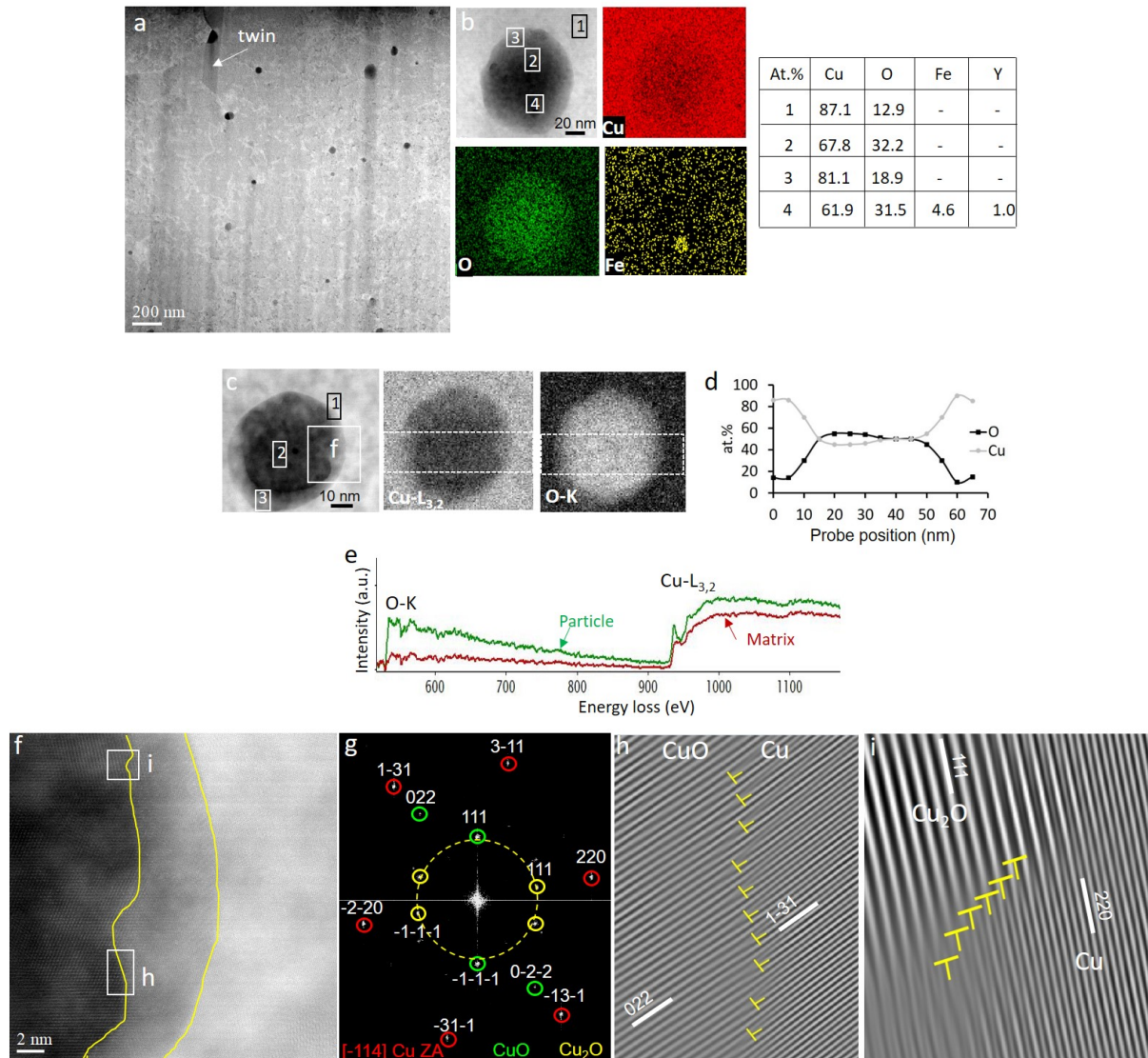
Figure 8: Cu-MG-3 nugget along the (XY) plane at a depth of 133 µm from the top surface. Low magnification HAADF image of the nugget showing the reinforcements distribution (a). Two of these fragments are presented in (b) and (c). For reinforcement (b), STEM-EDX elemental mapping has been performed and Cu K_α, O K_α and Fe K_α X-ray maps are displayed together with the relative atomic composition determined by EDX at various places located either in the particle or in its surroundings. Reinforcement (c) has been studied by STEM-EELS and the respective Cu $L_{3,2}$ and O K EELS maps are presented. Fig. (d) displays the Cu and O atomic profiles (d) through this (c) particle, while Fig. (e) shows EELS spectra for both the particle and the matrix extracted from the relevant spectrum image. Fig (f) is an HAADF image of a reinforcement – matrix interface (f) with the corresponding Fast Fourier transform pattern (g) and inverse Fast Fourier Transform images obtained using the selected reflections in (g) image with orientation relationships between both phases (h and i). In Fig (g), ZA stands for zone axis.

3.3.4.3. Nature of the reinforcements stemming from the primitive metallic glass and structure of their interfaces with the matrix

As shown by Fig. 9a for the Cu-MG-3 case, and irrespective of the number of passes, XRD analyses seem to unveil the existence of the FeB and Fe_2B compounds. This observation is

confirmed by the EPMA analyses of some particles with a stoichiometry close to $Fe_{2.37}B$ in the Cu-MG-3 sample (Fig. 9b).
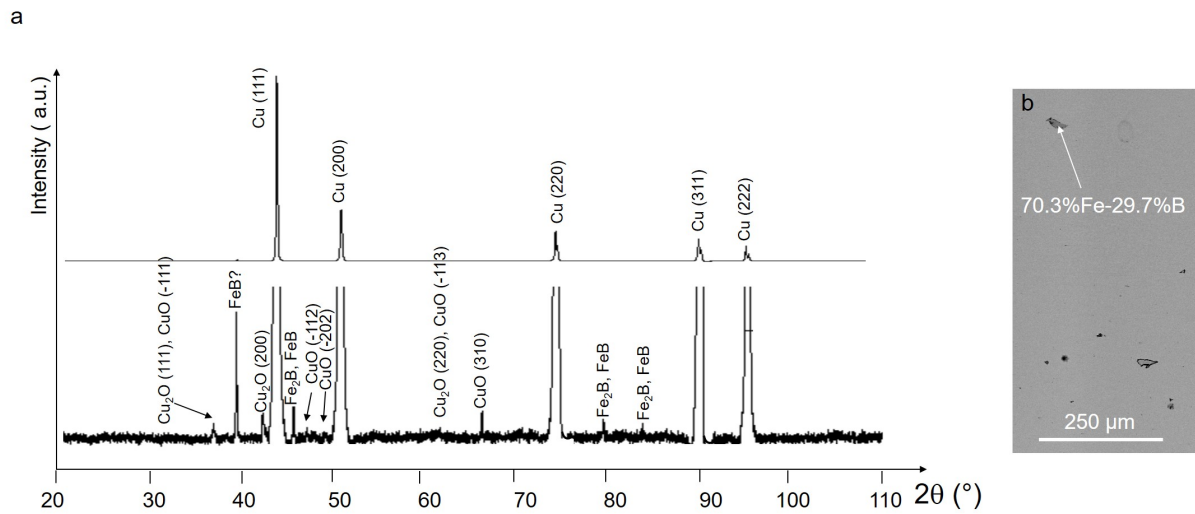

Figure 9: a) X-ray diffraction pattern of the Cu-MG-3 sample. Because of its low volume fraction, the amorphous MG cannot be detected in the FSP samples. b) BSE/SEM micrograph of the Cu-MG-3 transverse section and quantitative analysis (at.%) of a reinforcement by EPMA.

After one pass, STEM/EDX analyses (Fig. 10h-n) show that the reinforcements present Fe/Y, Fe/Nb and Y/Nb atomic ratios of 16.5, 12.4 and 0.92, respectively. These results are close to their 16, 10.7 and 0.67 ~~initial~~ primitive values in the initial metallic glass. In addition and still after the first pass, BSE micrographs of the Fe-B-Nb-Y-Al rich reinforcements reveal some bright contrasts (Fig. 7). These Fe and B bearing bright areas are Y free and enriched in Nb compared to the other parts of the reinforcement. They are also characterized by a Fe/Nb atomic ratio close to 0.51. The latter features of these bright zones recall the $Fe_3Nb_7B_8$ phase identified in the initial metallic glass after quenching [21]. During the first pass, Cu diffused towards and into the F-B-Nb-Y-Al rich fragments. The mean Cu content in the reinforcements is indeed 2.7 at.% (Fig 11a-b) and some subnanometric clusters with up to 17.8 at.% Cu are observed within the fragments (Fig. 11c-d). In this sample, the reinforcements analyzed in TEM are still amorphous. Indeed, the selected area electron diffraction pattern (SAEDP) of the reinforcement presents a diffuse and continuous ring corresponding to the 0.211 mean atom spacing (Fig. 10q). The 0.211 nm distance ~~of 0.211 nm~~ is close to 0.205 nm which is one of the two most frequent atomic spacings characteristic of the initial metallic glass [22]. In addition, Fig. 10a illustrates the presence of Nb, B, Y and O bearing reinforcements after three passes.

After the first pass, the matrix-reinforcement interface is bi-layered and amorphous according to the TEM analyses (Fig. 10h-p). As shown in Fig. 10k, going from the reinforcement to the matrix, the interface contains at first a 200 nm thick interfacial layer ~~with~~ containing about 12.0 at.% Fe, 9.9 at.% Nb, 5.0 at.% Cu and 73.0 at.% O followed by a 50 nm thick interfacial layer composed of around 24.6 at.% Fe, 59.0 at.% O and 6.4 at.% Cu. The SAEDP of the first interfacial layer presents a diffuse and continuous ring corresponding to the 0.334 nm most frequent atomic spacing (Fig. 10p). These rings unveil the existence of organized domains within the amorphous matrix. The distance of 0.334 nm is close to a characteristic distance of the $FeNbO_4$ crystal. It is worth noting that an oxidized Fe rich layer was also shown to surround a 30 µm sized and oxidized Nb-Y-B rich particle after 3 passes

12

(Fig. 10a-g). The oxygen rich layers covering the reinforcements may result from the imperfect contact of the Cu plates with the metallic glass ribbon in the initial stacking configuration.
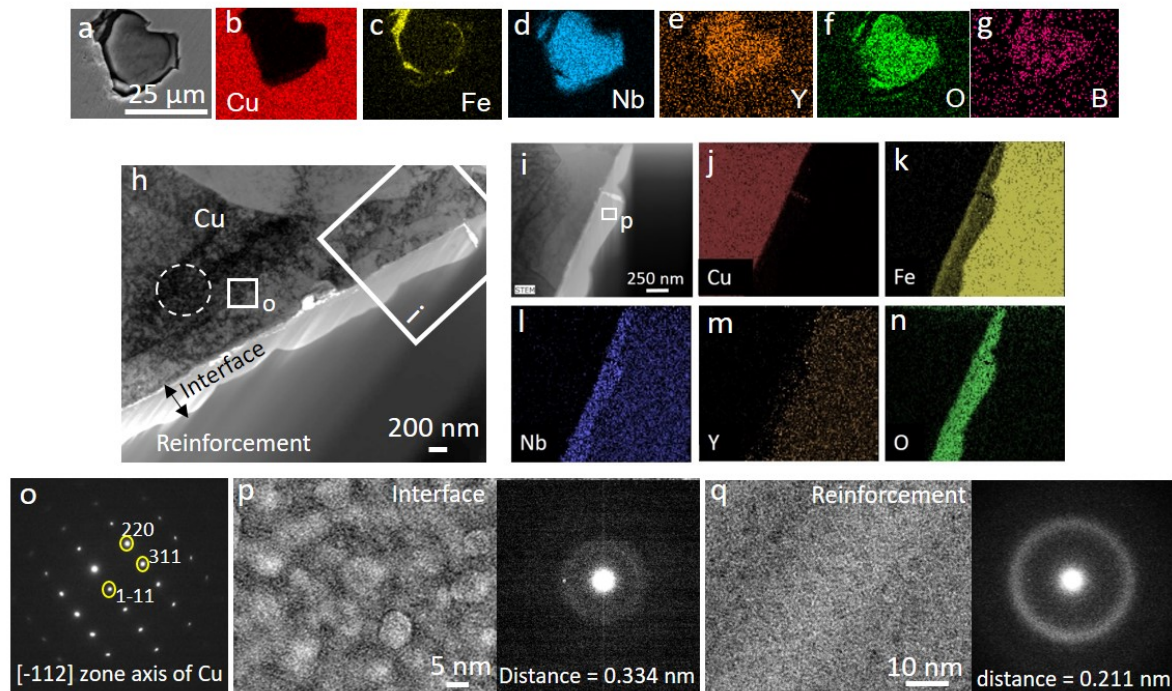

Figure 10: Transverse cross section of the Cu-MG-3 nugget: SEM image (a) and corresponding Cu K_α, Fe K_α, Nb K_α, Y K_α and O K_α X-ray maps (b-g). Nugget of the Cu-MG-1 along the (XY) plane: Bright field TEM image (h) of a Cu matrix – reinforcement interface in the nugget : the zone encircled by a dotted line points out the presence of entangled dislocations in Cu ; STEM image of the (i) zone in the (h) micrograph and corresponding Cu K_α, Fe K_α, Nb K_α, Y K_α and O K_α X-ray maps (j-n). Electron diffraction pattern of the (o) Cu grain part in Fig (h). Bright field TEM enlargement of 1) the zone (p) in the Cu-reinforcement interface in the (i) micrograph: (p) and of 2) the reinforcement (q) with their corresponding selected area electron diffraction patterns.
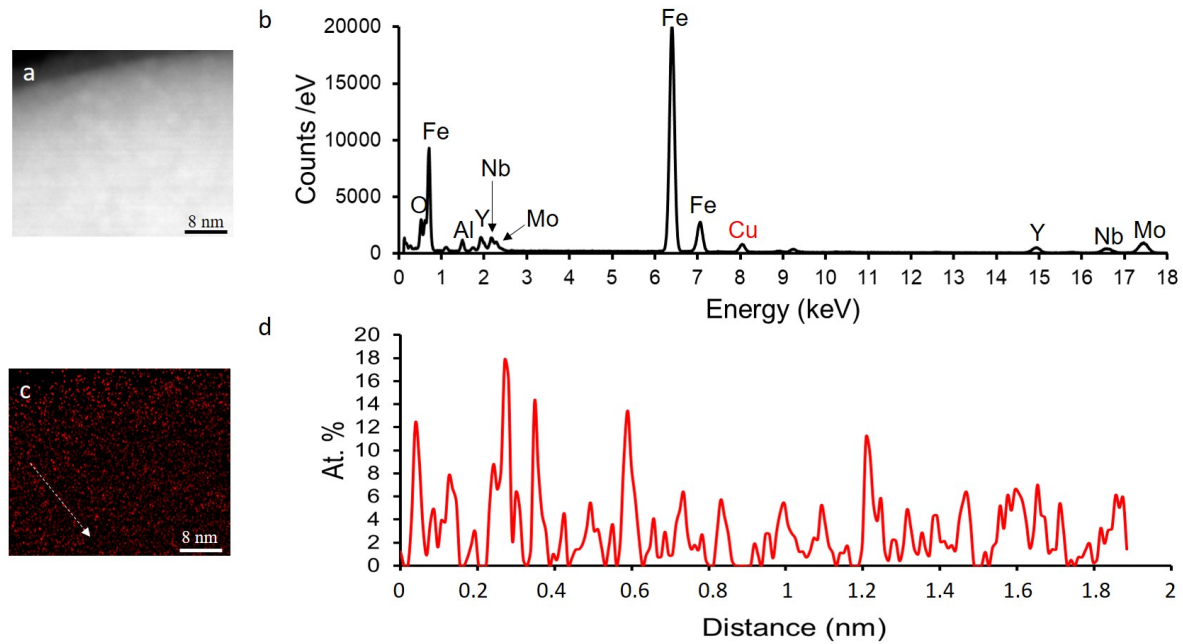
Figure 11: Cu-MG-1 sample: HAADF image inside a metallic glass reinforcement (a) with EDX spectrum (b), associated Cu K_α X-ray map (c) and Cu atomic profile (d) along the dashed white arrow drawn in figure c.

3.3.4.4. Oxidized reinforcements

Besides the reinforcements originating from the ~~initial~~ early metallic glass, some oxidized Cu particles are observed in the Cu matrix. After one pass, in the Cu-MG-1 sample, these spheroidal oxides present a size of about 5-6 µm (Fig. 12a-c). They contain 57.1 at.% Cu and 41.9 at.% O according to the EDX analyses which suggests an intermediate stoichiometry between CuO and Cu_2O. Their electron diffraction pattern identifies the Cu_2O phase (Fig. 12e) with inner nanometric particles (Fig. 12a and g-h) made of aggregates of crystals of Cu, CuO and Cu_2O (Fig. 12i). In the Cu-MG-3 nugget, the size of the spheroidal oxides has decreased since it reaches at most about 55 nm (Fig 8a). These reinforcements are again identified as the CuO compound according to EELS analyses (Fig. 8d and e) and as the Cu_2O phase according to more local EDX analyses (points 2 in Fig. 8). The oxidized particles present a nutshell which is slightly more oxidized than the Cu matrix (points 1 and 3, Fig. 8b and c). Some reinforcements contain 15 nm sized Fe rich particle (point 4, Fig. 8b) a priori stemming from the metallic glass or from an eventual contamination by the FSP tool. Electron diffraction patterns ascertain the presence of crystallites of both Cu_2O and CuO in these oxidized Cu particles (Fig. 8g). Inverse Fast Fourier Transform (FFT) further reveals some crystal orientation relationships, namely (111) Cu_2O // (220) Cu and (1-31) Cu // (022) CuO (Fig. 8h and i) with the presence of misfit dislocations at the interfaces. Different crystal orientation relationships were observed in the oxidized particles in the Cu-MG-1 sample, i.e. [-111] Cu // [1-10] Cu_2O and (220) Cu // (222) Cu_2O (Fig. 12i). Due to distinct states of stresses, the orientation relationships between Cu and the present Cu_2O embedded particles differ from those found for epitaxial oxidation, namely [111] Cu_2O // [111] Cu with (20-2) Cu_2O // (20-2) Cu **[45]** or [1-12] Cu // [0-11] Cu_2O **[46]**. Irrespective of the number of passes, and as exemplified after three FSP passes in Fig. 9, XRD analyses confirm the presence of the CuO and Cu_2O phases.

3.3.5. Cu matrix

The Cu matrix may contain some forests of dislocations as well as dislocation cells, at least locally (Fig. 12f). It is slightly oxidized as proved by EELS analyses (Fig. 8e), which may result from a slight oxidation of the thin foil surfaces.
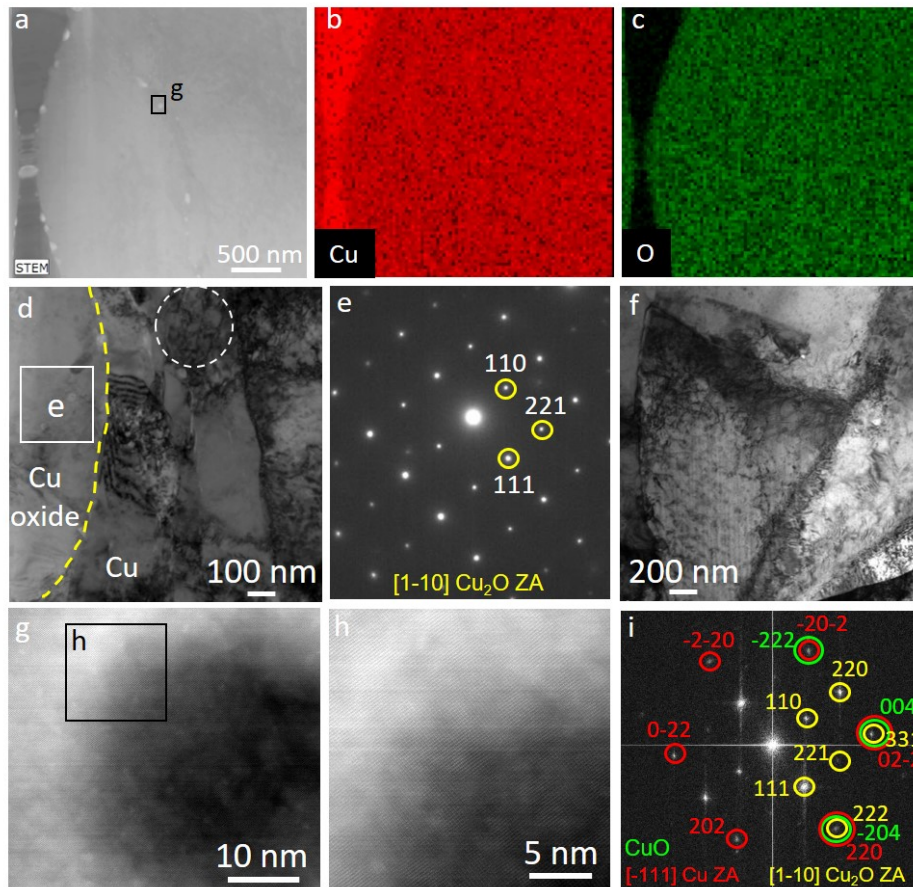

Figure 12: Bright field STEM image along an (XY) planar section of a part of a copper oxide particle contained inside the Cu matrix in the Cu-MG-1 nugget (a) and corresponding Cu Kα and O Kα X-ray maps (b-c). Aspect of the Cu grains surrounding the copper oxide particle which is delineated by the discontinuous yellow curve (d). Selected area electron diffraction pattern of the oxide particle corresponding to zone (e) in image (d). Dislocations arrangements inside the Cu grains (f). HAADF image of the nanometric particle marked by the g square in the (a) micrograph, and therefore inside the Cu oxide particle (g-h) with corresponding FFT pattern (i). The ZA abbreviation in Figs (e) and (i) stands for zone axis.

3.4. Microhardness

The microhardness maps depicted in Fig. 13 must be compared to the global microstructure in the transverse cross-section (Fig. 4d-f).

The Cu-no MG-1 nugget is shifted on the AS of the pin (Fig. 4d). It is harder than the HAZ but less strong than the base material (81 HV$_{0.05}$). The softening in both the nugget and the HAZ is due to Cu annealing which leads to coarser grain sizes in the HAZ (138 µm) than in the nugget (22 µm) and the base material (15 µm). Softening of the nugget has already been evidenced in the open literature during FSW of Cu despite a reduction of grain size [4,19]. It was explained by an annealing effect more important than ~~a~~ strain hardening ~~effect~~ [4,19].

With the MG ribbon addition, the microhardness is rather homogeneous in the nugget and the HAZ. After one pass ~~of FSP~~ (see the Cu-MG-1 sample map in Fig. 13) and whatever the ~~In these~~ zones, the hardness is close to ~~that of~~ the base material one. Only a very slight hardening is noted ~~at~~ in the nugget ~~surface~~. Due to the diminution of the nugget depth with the pass number (Fig 4e and 4f), ~~this apparent~~ near surface strengthening is somewhat more obvious with an increase of the number of passes. After three passes ~~of FSP, the top surface in the nugget is harder than the base material while~~ the HAZ is clearly the weakest zone (see the ~~map of~~ Cu-MG-3 sample map, Fig. 13).

Irrespective of the sample, HAZ softening ~~of the HAZ~~ results from Cu annealing. The refinement of the mean grain size ~~in the nugget~~, i.e. 22 µm in Cu-no MG-1, 3.4 µm in Cu-MG-1 and 1.9 µm in Cu-MG-3, is a priori consistent with the ~~small~~ nugget hardening ~~of this zone~~. The distribution of the second phases and the effect of the ~~number of FSP~~ passes number on the deformation substructure are additional strengthening parameters. Due to a too large particle spacing, the intragranular second phases distribution ~~has~~ exerts however a small hardening effect in the nugget. A far higher volume fraction of metallic glass should be inserted in Cu in order to obtain a significant dispersion hardening. Because of their low frequency (Fig. 5d), the twins also do not seem to play a significant role on the hardening of the nuggets.
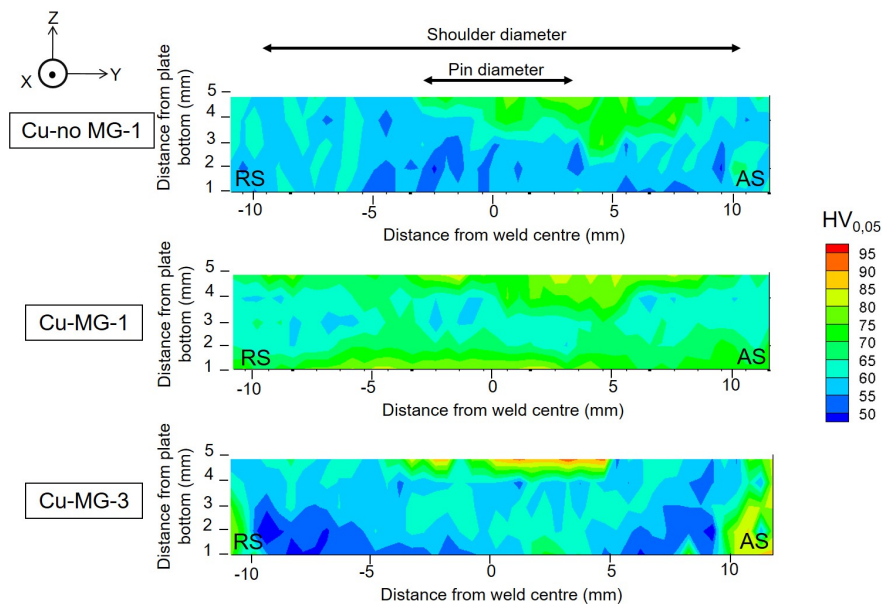

Figure 13: 50 g Vickers microhardness maps in the transverse cross section of the Cu-no MG-1, Cu-MG-1 and Cu-MG-3 samples. The measurement step spacing was 500 µm along the Y axis and 1 mm along the Z axis.

4. Discussion

4.1. Dynamic recrystallization and dynamic recovery

Copper is known to present a stacking fault energy of 80 mJ/m² at room temperature, which is medium among face centered cubic metals [29,47], and causes slow recovery phenomena [29]. For Cu deformed at high temperature, i.e. at homologous temperatures greater than 0.5, restoration occurs by dynamic recovery and/or dynamic recrystallization [29].

As displayed in Fig 6d-e, some 3-4 µm sized and thus large second phases are surrounded by nanometric recrystallized copper grains. Dynamic recrystallization was very likely favored by 1) the accumulation of dislocations at the surroundings of reinforcements since these second phases act as obstacles to the material flow during processing and 2) the slowness of the recovery processes in Cu. Highly misoriented deformation zones associated with these coarse particles lead to a wide range of nuclei orientations [29].

Some dislocations cells (encircled in Figs. 10h and 12d) are also detected in Cu. This proves the effectiveness of recovery at least locally along the process. The phenomenon is dynamic or static if it occurs during the process or ~~after~~in the tool ~~path~~wake, respectively.

4.2. New phases generated during FSP

Among the various new phases developed during FSP, it is worth noting that no tool fragment due to an eventual contamination has been detected in the processed samples.

4.2.1. Behavior and evolution of the metallic glass

4.2.1.1 Fragmentation
During FSP, the metallic glass ribbon is fragmented into more or less coarse and angular pieces (Figs. 6 and 7). An increase of the pass number was further shown to reduce the ~~size of~~ reinforcements size (Fig. 7). This fragmentation has very likely occurred from the very beginning of the processing cycle when the tool entered into contact with the brittle glassy ribbon whose hardness is close to 1027 $HV_{0.05}$ at ambient temperature. Similar behaviors of bulk metallic glasses are reported in the friction stir butt welding literature. For instance, some particles of untransformed bulk MG were stirred into the Al alloy during dissimilar butt friction stir welding of a $Zr_{55}Cu_{30}Al_{10}Ni_5$ bulk metallic glass (BMG) to a 7075 Al alloy ~~butt FSW~~ with a tool pin offset into the Al side and a 12.5% pin width ~~of the pin~~ into the metallic glass [20]. Some irregular fragments with various sizes of ~~the~~ untransformed ~~$Zr_{55}Cu_{30}Al_{10}Ni_5$~~ metallic glass were also detected on the Cu side for the case of the Cu-$Zr_{55}Cu_{30}Al_{10}Ni_5$ butt friction stir welding with a slight contact of the tool with the bulk MG [19].

The microstructural analyses do not exhibit any sign of viscous flow for the metallic glass. This suggests a processing temperature a priori below the glass transition temperature (585°C with a heating rate of 10°C/min) or higher than the primary crystallization temperature (677°C with a heating rate of 10°C/min).

4.2.1.2 Cu diffusion and phase transformations in the metallic glass~~MG~~
Proofs of crystallization of the Fe based MG were given by XRD (Fig. 9a), EDX/SEM ~~analyses~~ (Fig. 10a) and EPMA (Fig. 9b) analyses. Some FeB and Fe_2B crystals in both the Cu-MG-1 and Cu-MG-3 samples as well as Nb-B-Y-O bearing particles in Cu-MG-3 were detected ~~in Cu MG 3~~. Thus some glassy reinforcements have locally reached at least the primary crystallization temperature.

Those signs of crystallization could supply an indication on the temperature reached during FSP. Avettand-Fènoël et al. [21] have shown that at a heating rate of 10°C/min and without any deformation, the glass transition and primary crystallization temperatures are of 585 and 677°C, respectively for the present metallic glass. Besides, it is well-known that, under deformation, phase transformations may occur at temperatures lower than the equilibrium ones [48]. Nevertheless, in the present study, deformation of the MG was not observed during the process, even if the brittle fracture of the metallic glass has very likely been preceded by the fast formation of shear bands. Indeed, no sign of viscous flow associated

to a supercooled state or of shear bands was detected in the glass. Then only two factors may very likely have promoted phase transformations into the metallic glass, namely the heating during the FSP thermal cycle and the Cu diffusion into the MG.

Concerning the single effect of temperature, the nature of the crystallized phases formed during FSP can be compared with those formed during the isothermal annealing of the considered MG. As aforesaid, during FSP, the homologous temperature is close to 0.6 – 0.7, which leads to a processing temperature in-between 550°C and 688°C for Cu. Yet, XRD, HRTEM and atom probe tomography analyses evidenced the crystallization of FeB, $Fe_{2.4}B$ and $Fe_{62}B_{14}Y_3$ after 667°C annealing of the $Fe_{64}B_{24}Y_4Nb_6Al_{0.4}$ metallic glass subsequent to a heating rate of 10°C/min [22]. At this temperature, an incubation time shorter than 1 min was also required for crystallization to start [22]. Except the binary iron borides detected by XRD and EPMA in the FSP sample, the ternary $Fe_{62}B_{14}Y_3$ phase was not identified, while once nucleated, its growth kinetics is high at 667°C. This suggests that the incubation time of crystallization of the latter phase was not reached at the FSP processing temperature. It is very likely due to the very few seconds, and thus too short duration spent by the material at the peak temperature (very few seconds) and to the high thermal diffusivity of Cu (117×10^{-6} m²/s). ~~or~~ It could also mean that the material did not reach 667°C during FSP. Instead, some Nb-Y-O-B bearing particles were detected (Fig. 10a-g), which proves that their formation was more favored at the processing temperature. By comparison with literature, there exists some cases where ~~the~~ a MG did not crystallize at all during FSP [19]. Indeed, despite a processing peak temperature higher than that of the $Zr_{55}Cu_{30}Al_{10}Ni_5$ MG peak of crystallization, no MG crystallization was for instance observed during FSW of bulk MG – Cu [19]. This was explained by the time-dependent nucleation of the crystalline phases which requires an incubation period of 1 min, and thus longer than the few seconds spent at the processing peak ~~welding~~ temperature and all the more that Cu cools rapidly because of its~~has a~~ high thermal diffusivity.

It is also relevant to question about (i) the presence of Cu clusters into the reinforcements and (ii) an eventual role played by Cu on the primary crystallization of the MG during FSP.

Firstly, Fig. 11 exhibited local Cu enrichments into some MG reinforcements which have remained at the amorphous state. Cu diffusion into these fragments suggests that they have reached a temperature in-between the glass transition and the primary crystallization temperatures despite the absence of obvious viscous flow sign. Actually, compared to the glassy state where ~~the~~ atomic diffusion depends on the free volume in the glass and needs ~~can occur provided it results from a~~ local cooperative atomic ~~motion~~ rearrangements [49-50], atomic diffusion should be easier at the supercooled state.

Secondly, the Fe-Cu, B-Cu, Nb-Cu and Y/Cu heats of mixing are ~~respectively~~ 13 kJ/mol [23], 0 [23] or 15 kJ/mol [51], 3 kJ/mol [23] and -22 kJ/mol [23], respectively. Therefore, Cu is repelled by Fe, Nb and very likely B but attracted by Y. In agreement with the positive heat of mixing between Fe and Cu, literature has reported different studies showing the behavior of Cu in Cu bearing Fe based metallic glasses. The dispersion of fcc-Cu nanocrystals containing stacking faults was for instance exhibited in $(Fe_{0.75}Nb_{0.10}B_{0.15})_{80}Cu_{20}$ melt-spun metallic glasses ribbons [51].

Thirdly, Cu is known to reduce the glass forming ability (GFA) of the Fe based metallic glasses [23]. The addition of 0.5 or 1 at.% Cu to $Fe_{0.71}Nb_{0.06}B_{0.23}$ was shown to lead to the in-situ crystallization of 8 and 32 vol.%~~respectively~~ of bcc-Fe and $Fe_{23}B_6$ nanocrystals in the as-cast metallic glass, respectively [52]. In the same way, the replacement of 1 at.% Nb by Cu in the $Fe_{75}Nb_{10}B_{15}$ composition was shown to increase the bcc-Fe nucleation rate, and thus to decrease the crystallization temperature of the Fe based amorphous alloy [53]. The

enhancement of nanocrystallization in Fe based MG by the presence of Cu was explained by either the formation of Cu clusters acting as heterogeneous nucleation sites for primary nanocrystals such as in FINEMET alloys, with Fe(Ni)NbCu(Si)B compositions like for instance 80 Fe – 6 Si – 3 Nb - 1 Cu – 10 B (at.%)), or by the partitioning of the Cu bearing MG structure, such as in the $Fe_{84}Nb_7B_9Cu_x$ case, into a major Fe-Nb-B based amorphous phase and a minor Cu containing amorphous phase divided in "like-bcc clusters" acting as nucleation sites for bcc-Fe primary crystals [53]. A similar behavior of Cu may be proposed in the present work even if no concomitant Cu clustering and crystals nucleation in the MG were observed after FSP.

4.2.1.3 Second phase / matrix interface

The microstructure of the interfaces between the second phases and the matrix (Fig. 10h) proves once again that atomic interdiffusion has occurred between the matrix and the metallic glass during FSP. Indeed, oxidized and amorphous interlayers enriched in Fe, Cu and eventually Nb are identified at the reinforcement – matrix interfaces. The presence of such thin interfaces enables a suitable atomic bonding between the reinforcements and the matrix. But the amorphous nature of these interfaces questions about their ductility and thermal stability.

Conversely, in another work dealing with the butt FSW of $Zr_{55}Cu_{30}Al_{10}Ni_5$ bulk MG to Cu, microvoids were observed instead of a transition layer at the MG fragments – Cu interfaces [19]. The authors explained their presence by the different volume shrinkage of both phases when cooled from the high temperature.

4.2.2. Copper oxide particles

The presence of copper oxides particles inside the Cu matrix is very likely due to oxygen contamination along the process despite the presence of an argon flux. This contamination is probably enhanced by the material flow. A free space is indeed left behind the tool during its advance before gap filling by the retreating material [54]. These oxides are essentially composed of CuO crystallites together with some Cu_2O ones (Fig. 8 and 12). According to the Ellingham's diagram, the heat of formation of CuO and Cu_2O is $\Delta G°_f$ (CuO) = -66.6 kJ/mol and $\Delta G°_f$ (Cu_2O) = -95.5 kJ/mol, respectively at a temperature of 727°C, respectively [55]. 727°C is close to the expected 550°C to 688°C processing temperature as FSW proceeds at a 0.6 to 0.7 homologous temperature. Therefore, Cu_2O forms more easily than CuO. In addition, according to literature [56,57], the sequence of oxidation of Cu is Cu→Cu_2O→CuO and CuO formed at the expense of Cu_2O at temperatures greater than 320°C in equilibrium conditions. This information suggests that the temperature was higher than 320°C in the zones where such oxides have formed.

5. Conclusions

Multipass friction stir processing was successfully performed on Cu plates stacked on both faces of a $Fe_{64}B_{24}Y_4Nb_6Al_{0.4}$ metallic glass ribbon. The following results have been obtained:
-   The brittle metallic glass ribbon fractured into micrometric and even nanometric fragments during the process, and all the more with an increase of the number of passes. These fragments were shown to disturb the material flow during processing. They promote the formation of vortices and bands with different levels of deformation generating small grains zones next to coarse grains areas in the nugget.

- From the first FSP pass, some fragments of metallic glass partially crystallized into iron borides and Nb-B-Y-O bearing particles.
- Some other fragments of metallic glass remained amorphous. They were shown to contain some local Cu clusters in agreement with the Fe-Cu positive heat of mixing. The Cu diffusion into these reinforcements suggests that the temperature reached during the process is at least the glass transition temperature.
- The interface of the Cu matrix with the metallic glass based reinforcements is amorphous, 250 nm thick and bilayered. From the reinforcement towards the matrix, the interfacial layers are successively made of an oxide of Fe, Nb and Cu and an oxide of Fe and Cu.
- Some nanometric polycrystalline copper oxides were also formed and dispersed in the nugget and the Cu_2O/Cu and CuO/Cu crystallographic orientation relationships have been obtained.
- The nugget experienced dynamic recovery and dynamic recrystallization which was in particular favored around the MG fragments.
- The greater the number of passes, the harder the nugget is.

Acknowledgments

References

[1]   X.C. Liu, Y.F. Sun, T. Nagira, K. Ushioda, H. Fujii, Strain rate dependant micro-texture evolution in friction stir welding of copper, Materialia 6 (2019) 100302

[2]   A. Heidarzadeh, H.M. Laleh, H. Gerami, P. Hosseinpour, M.J. Shabestari, R. Bahari, The origin of different microstructural and strengthening mechanisms of copper and brass in their dissimilar friction stir welded joint, Mater. Sci. Eng. A 735 (2018) 336-342

[3]   A. Heidarzadeh, T. Saeid, V. Klemm, A. Chabok, Y. Pei, Effect of stacking fault energy on the restoration mechanisms and mechanical properties of friction stir welded copper alloys, Mater. Design 162 (2019) 185-197

[4]   Y.F. Sun, H. Fujii, Investigation of the welding parameter dependent microstructure and mechanical properties of friction stir welded pure copper, Mater. Sci. Eng. A 527 (2010) 6879-6886

[5]   Y. Wang, R. Fu, L. Jing, Y. Li, D. Sang, Grain refinement and nanostructure formation in pure copper during cryogenic friction stir processing, Mater. Sci. Eng. A 703 (2017) 470-476

[6]   J.Q. Su, T.W. Nelson, T.R. McNelley, R.S. Mishra, Development of nanocrystalline structure in Cu during friction stir processing (FSP), Mater. Sci. Eng. A 528 (2011) 5458-5464

[7]   P. Xue, B.L. Xiao, Z.Y. Ma, Achieving large-area bulk ultrafine grained Cu via submerged multiple-pass friction stir processing, J. Mater. Sci. Technol. 29(12) (2013) 1111-1115

[8]   P. Xue, B.B. Wang, F.F. Chen, W.G. Wang, B.L. Xiao, Z.Y. Ma, Microstructure and mechanical properties of friction stir processed Cu with an ideal ultrafine-grained structure, Mater. Charact. 121 (2016) 187-194

[9] H. Mazaheri, H.J. Aval, R. Jamaati, Achieving high strength-ductility in pure copper by cold rolling and submerged friction stir processing (SFSP), J. Manuf. Proc. 67 (2021) 496-502

[10] M.-N. Avettand-Fènoël, A. Simar, R. Shabadi, R. Taillard, B. de Meester, Characterization of oxide dispersion strengthened copper based materials developed by friction stir processing, Mater. Design, 60 (2014) 343-357

[11] R. Sathiskumar, N. Murugan, I. Dinaharan, S.J. Vijay, Prediction of mechanical and wear properties of copper surface composites fabricated using friction stir processing, Mater. Design 55 (2014) 224–34.

[12] M. Barmouz, M.K.B. Givi, Fabrication of in-situ Cu/SiC composites using multipass friction stir processing: evaluation of microstructural, porosity, mechanical and electrical behavior, Composites: Part A 42 (2011) 1445–53.

[13] M. Barmouz, P. Asadi, M.K. Besharati Givi, M. Taherishargh, Investigation of mechanical properties of Cu/SiC composite fabricated by FSP: effect of SiC particles' size and volume fraction, Mater. Sci. Eng. A 258 (2011) 1740–9.

[14] M. Barmouz, M.K. Besharati Givi, J. Seyfi, On the role of processing parameters in producing Cu/SiC metal matrix composites via friction stir processing: investigating microstructure, microhardness, wear and tensile behavior, Mater. Charact. 62 (2011) 108–17.

[15] Y.F. Sun, H. Fujii, The effect of SiC particles on the microstructure and mechanical properties of friction stir welded pure copper joints, Mater. Sci. Eng. A 528 (2011) 5470–5.

[16] M.R. Akbapour, E. Salahi, F. Alikhani Hesari, H.S. Kim, A. Simchi, Effect of nanoparticle content on the microstructural and mechanical properties of nano-SiC dispersed bulk ultrafine-grained Cu matrix composites, Mater. Design 52 (2013) 881–7.

[17] H.R. Akramifard, M. Shamanian, M. Sabbaghian, M. Esmailzadeh, Microstructure and mechanical properties of Cu/SiC metal matrix composite fabricated via friction stir processing, Mater. Design 54 (2014) 838–44.

[18] A. Saadati, M. Malekan, F. Khodabakhshi, Under glass transition temperature diffusion bonding of bulk lmetallic glass and aluminum, Mater. Chem. Phys. 269 (2021) 124758

[19] Y. Sun, Y. Ji, H. Fujii, K. Nakata, K. Nogi, Microstructure and mechanical properties of friction stir welded joint of Zr50Cu30Al10Ni5 bulk metallic glass with pure copper, Mater. Sci. Eng. A 527 (2010) 3427-3432

[20] D. Wang, B.L. Xiao, Z.Y. Ma, H.F. Zhang, Friction stir welding of $Zr_{55}Cu_{30}Al_{10}Ni_5$ bulk metallic glass to Al-Zn-Mg-Cu alloy, Scripta Mater. 60 (2009) 112-115

[21] M.-N. Avettand-Fènoël, M. Marinova, R. Taillard, W. Jiang, Thermal stability, phase transformations and mechanical properties of a $Fe_{64}B_{24}Y_4Nb_6$ metallic glass, J. All. Compnds. 854, 2021, 157068, 1-15

[22] M.-N. Avettand-Fènoël, X. Sauvage, M. Marinova, A. Addad, Multiscale investigation of the crystallization mechanisms and solute redistribution during annealing of a $Fe_{64}B_{24}Y_4Nb_6Al_{0.4}$ metallic glass, J. All. Compnds. 887 (2021) 161264

[23] A. Takeuchi, A. Inoue, Classification of bulk metallic glasses by atomic size difference, heat of mixing and period of constituent elements and its application to characterization of the main alloying element, Mat. Trans. 46(12) (2005) 2817-2829

[24] B. Beausir and J.-J. Fundenberger, Analysis Tools for Electron and X-ray diffraction, ATEX - software, www.atex-software.eu, Université de Lorraine - Metz, 2017

[25] H. Miura, T. Sakai, S. Andiarwanto, J.J. Jonas, Nucleation of dynalmic recrystallization at triple junctions in polycrystalline copper, Phil. Mag. 85 (2005) 2653-2669

[26] K. Han, R.P. Walsh, A. Ishmaku, V. Toplosky, L. Brandao, J.D. Embury, High strength and high electrical conductivity bulk Cu, Phil. Mag. 84 (34) (2004) 3705-3716

[27] C.X. Huang, K. Wang, S.D. Wu, Z.F. Zhang, G.Y. Li, S.X. Li, Deformation twinning in polycrystalline copper at room temperature and low strain rate, Acta Mat. 54 (2006) 655-665

[28] H.J. Liu, J.J. Shen, Y.X. Huang, L.Y. Kuang, C. Liu, C. Li, Effect of tool rotation rate on microstructure and mechanical properties of friction stir welded copper. Sci. Technol. Weld. Join. 14(6) (2009) 577-583

[29] F.J. Humphreys, M. Hatherly, Recrystallization and related annealing phenomena, Pergamon, Elsevier Science, Oxford, 1995

[30] A. Arora, Z. Zhang, A. De, T. DebRoy, Strains and strain rates during friction stir welding, Scripta Mater. 61 (2009) 863–66

[31] P. Heurtier, C. Desrayaud, F. Montheillet, A thermomechanical analysis of the friction stir welding process, Mater. Sci. Forum 396-402 (2002) 1537–1542

[32] H. Schmidt, J.H. Hattel, A local model for the thermomechanical conditions in friction stir welding, Modell. Simul. Mater. Sci. Eng. 13 (2005) 77–93

[33] G. Buffa, J. Hua, R. Shivpuri, L. Fratini, Design of the friction stir welding tool using the continuum based FEM model, Mater. Sci. Eng. A. 419 (2006) 381–388

[34] G. Buffa, J. Hua, R. Shivpuri, L. Fratini, A continuum based fem model for friction stir welding – model development, Mater. Sci. Eng. A. 419 (2006) 389–396

[35] K. Masaki, Y.S. Sato, M. Maeda, H. Kokawa, Experimental simulation of recrystallized microstructure in friction stir welded Al alloy using a plane-strain compression test, Scripta Mater. 58 (2008) 355–360

[36] M. Militzer, W.P. Sun, J.J. Jonas. Modelling the effect of deformationinduced vacancies on segregation and precipitation, Acta Metall. Mater. 42 (1994) 133–141

[37] Gunduz 2005 I.E. Gunduz, T. Ando, E. Shattuck, P.Y. Wong, C.C.Doumanitis.Enhanced diffusion and phase transformations during ultrasonic welding of zinc and aluminum, Scripta Mater. 52 (2005) 939–943

[38] R.S. Mishra, Z.Y. Ma, Friction stir welding and processing, Mater. Sci. Eng.R, 50 (2005) 1–78

[39] R. Nandan, T. DebRoy, H.K.D.H. Bhadeshia, Recent advances in friction stir welding –Process, weldment structure and properties, Progr. Mater. Sci., 53 (2008) 980 1023

[40] K.V. Jata, S.L. Semiatin, Continuous dynamic recrystallization during friction stir welding of high strength aluminum alloys, Scripta Mater. 43 (2000) 743–749

[41] Ø. Frigaard, Ø. Grong, O.T. Midling, A process model for friction stir welding of age hardening aluminum alloys, Metall. Mater. Trans. A 32A (2001) 1189–1200

[42] A. Gerlich, G. Avramovic-Cingara, T.H. North, Stir zone microstructure and strain rate during Al 7075-T6 friction stir spot welding, Metall. Mater. Trans. A 37A (2006) 2773–2786

[43] C.I. Chang, C.J. Lee, and J.C. Huang, Relationship between grain size and Zener Hollomon parameter during friction stir processing in AZ31 Mg alloys, Scripta Mater. 51 (2004) 509–514

[44] A. Askari, S. Silling, B. London, M. Mahoney, Friction Stir Welding and Processing, TMS, Warrendale, PA (2001) 43–54

[45] A. Altaweel, Synthèse de nanostructures d'oxyde de cuivre par micro-post-décharge micro-ondes à pression atmosphérique, PhD, Université de Lorraine, 2014

[46] L. Yuan, Q. Yin, Y. Wang, G. Zhou, CuO reduction induced formation of CuO/Cu_2O hybrid oxides, Chem. Phys. Lett. 590 (2013) 92-96

[47] K. Huang, R.E. Logé, A review of dynamic recrystallization phenomena in metallic materials, Mater. Design 111 (2016) 548-574

[48] A. Anghelus, M.-N. Avettand-Fènoël, C. Cordier, R. Taillard, Microstructural evolution of aluminium/ Al-Ni-Sm glass forming alloy laminates obtained by controlled accumulative roll-bonding, J. All. Compnds 631 (2015) 209-218

[49] S.V. Ketov, Y.P. Ivanov, D. Sopu, D.V. Louzguine-Luzgin, C. Suryanarayana, A.O. Rodin, T. Schöberl, A.L. Greer, J. Eckert, High-resolution transmission electron microscopy investigation of diffusion in metallic glass multilayer films, Mater. Today Adv. 1 (2019) 100004

[50] A. Annamareddy, P.M. Voyles, J. Peperezko, D. Morgan, Mechanisms of bulk and surface diffusion in metallic glasses determined from molecular dynamics simulations, Acta Mater. 209 (2021) 116794

[51] T. Nagase, M. Suzuki, T. Tanaka, Formation of amorphous phse with crystalline globules in Fe-Cu-Nb-B immiscible alloys, J. All. Compnds. 619 (2015) 267-274

[52] J.M. Park, D.H. Kim, J. Eckert, Enhanced plasticity of Fe-Nb-B-(Ni,Cu) bulk metallic glasses by controlling heterogeneity and elastic constants, J. All. Compnds. 536S (2012) S70-S73

[53] J. Torrens-Serra, P. Bruna, J. Rodriguez-Viejo, S. Roth, M.T. Clavaguera-Mora, Effect of minor additions on the glass forming ability and magnetic properties of Fe-Nb-B based metallic glasses, Intermetallics 18 (2010) 773-780

[54] M. Guerra, C. Schmidt, J.C. McClure, L.E. Murr, A.C. Nunes, Flow patterns during friction stir welding, Mater. Charact. 49 (2003) 95-101

[55] Smithells Metals Reference Book, seventh edition, Eds.: E.A. Brandes, G.B. Brook, Butterworth Heinemann, Oxford, 1992

[56] C. Choudhary, J.V.N. Sarma, S. Pande, S. Ababou-Girard, P. Turban, B. Lepine, S. Gangopadhyay, Oxidation mechanism of thin Cu films: a gateway towards the formation of single oxide phase. AIP Advances 8, 055114 (2018) https://doi.org/10.1063/1.5028407

[57] C. Zheng, J. Cao, Y. Zhang, H. Zhao, Insight into the oxidation mechanism of a Cu-based oxygen carrier (Cu→Cu_2O→CuO) in chemical looping combustion, Energy Fuels 34(7) (2020) 8718-8725